Sensors and Materials, Vol. 38, No. 8 (2026) 4655–4672
MYU Tokyo

S & M 4587

Frequency-modulated Continuous-wave-based Distributed Sensing System for Partial Insulation Defect Localization in Distribution Cables: Impact on Connected Electrical Equipment

Dewen Zhang,* Mingyu Xu, Ruihui Han, Jie Sheng, Ziheng Wang, and Zhongyu Wang

The State Grid Heilongjiang Electric Power Research Institute, Harbin, Heilongjiang Province 150030, China

(Received May 11, 2026; accepted August 12, 2026)

Keywords: power distribution cables, FMCW, insulation defect localization, transformer high-frequency equivalent model, impedance matching

The accurate localization of partial insulation defects in cross-linked polyethylene (XLPE) distribution cables is critical for condition-based maintenance in smart power grids. In this study, we developed a frequency-modulated continuous wave (FMCW) diagnostic method that treats the cable as a distributed impedance sensor, enabling noninvasive detection under energized conditions. High-frequency current transformers and high-voltage coupling capacitors provide safe signal injection and extraction. Experiments on an energized 8.7/10 kV YJV cable (copper conductor cable with XLPE insulation and polyvinyl chloride sheath) demonstrate that the FMCW method achieves consistent localization accuracy, with a measured defect at 22.18 m (standard deviation = 0.11 m), which corresponds to a relative error of only 0.82% across 30 repeated trials. Transformer integration reduced the terminal reflection peak amplitude by 7.768%, and the defect-induced reflection peak decreased by only 0.836%, confirming that defect reflections act as independent scattering centers decoupled from boundary perturbations. Localization error remained stable at approximately 5% under both isolated and transformer-coupled conditions. These results indicate the robustness of FMCW sensing against terminal impedance variations and highlight its superiority over conventional reflectometry methods. The results of this study provide a theoretical basis for deploying FMCW-based distributed sensing systems in resilient power distribution networks, enabling the reliable online monitoring of insulation health under practical operating conditions.

1. Introduction

With the rapid pace of urbanization, distribution networks must be continuously expanded to meet growing energy demands. In China, the fault rate of distribution networks has increased every year, despite ongoing efforts. Such an increase in fault rate underscores the need for defect localization technologies to detect and locate early-stage defects to prevent catastrophic failures.

*Corresponding author: e-mail: dewen1984@163.com
https://doi.org/10.18494/SAM6422

ISSN 0914-4935
https://myukk.org/

In modern urban systems, cross-linked polyethylene (XLPE) cables are predominantly used for power transmission owing to their excellent insulation properties, high reliability, and compact installation requirements.[1,2] However, even XLPE cables are affected by long-term electrical stress, thermal cycling, mechanical vibration, moisture ingress, and sheath damage. Although such defects are latent for extended periods, they eventually degrade the insulation of the cable and cause severe defects, including breakdowns and short circuits, threatening the reliability and safety of power systems.[3,4] Along with the defects on the cable, the increasing complexity of smart grids requires condition-based maintenance rather than conventional periodic maintenance. Condition-based maintenance necessitates advanced sensing technologies, since conventional physical sensors often cannot provide localized defect information. This leads to the development of reflectometry-based approaches that utilize the cable as a distributed sensing medium.[5] Consequently, high-sensitivity, high-accuracy, and online cable defect localization methods must be developed for efficient condition-based maintenance and grid resilience.

In cable defect monitoring, time-domain reflectometry (TDR) and frequency-domain reflectometry (FDR) methods are used. In the TDR method, the most widely used technique, short-duration pulses injected into the cable are detected, and reflections caused by impedance discontinuities are analyzed to locate defects.[6,7] While effective for severe defects such as open circuits and short circuits, the TDR method has limited sensitivity to weak insulation defects owing to insufficient high-frequency components, strong signal attenuation, and susceptibility to noise in complex electromagnetic environments.[8,9] To address these limitations, the FDR method has been proposed. In the FDR method, broadband impedance spectroscopy (BIS) is widely used owing to its superior sensitivity to local impedance variations.[10,11] By analyzing frequency-dependent impedance characteristics, BIS detects subtle parameter changes associated with insulation degradation. The FDR method outperforms the TDR method in locating weak defects and assessing insulation aging,[12,13] but BIS requires long sweeping time, typically tens of minutes, and is sensitive to noise, limiting its adoption for field applications and online monitoring.

To enhance measurement efficiency and noise immunity, a frequency-modulated continuous-wave (FMCW)-based method has been developed as an advanced FDR method.[6] Mimicking radar signal processing, the FMCW method employs linearly frequency-modulated signals to convert propagation delay into frequency differences, enabling the accurate distance estimation of impedance discontinuities.[14,15] Widely applied in high-precision sensing, such as light detection and ranging, the FMCW method enables the nondestructive detection of structural variations in dielectric materials such as XLPE.[16] Compared with BIS-based methods, the FMCW method reduces measurement time from 30–60 s down to 1–3 s, provides higher noise immunity across high electromagnetic interference (EMI) environments, and extends the effective detection range up to 1.5 km.[7] The FMCW method increases the effective detection range by more than 30% compared with that of the BIS-based method under the same bandwidth conditions.[14] By introducing matched filtering and optimized mixing strategies, detection sensitivity and resolution can be significantly enhanced by using the FMCW method,[17,18] which makes the FMCW method well-suited for early-stage insulation defect localization in long distribution cables.

In distribution networks, cables are connected to transformers, switchgear, and other terminal equipment that introduce parasitic impedance and distort reflection characteristics. As a result, integrating high-frequency sensing interfaces such as high-frequency current transformers or capacitive couplers into energized systems is challenging, since the FMCW method performs best under ideal terminal impedance and simplified boundary conditions. For defect localization in real power distribution networks, diagnostics must be conducted without interrupting power supply, must withstand strong electromagnetic interference from power-frequency fields and harmonics, and must ensure the safe injection and extraction of high-frequency signals from high-voltage cables. Although electromagnetic and capacitive coupling techniques are applied in conventional FDR methods,[19,20] their adaptation to FMCW-based localization and the associated sensor development remain insufficiently explored. Moreover, the effect of connected electrical equipment on measurements using the FMCW method must be clarified, since transformers and other terminal devices alter impedance boundary conditions, which suppress reflection peaks or introduce spectral distortions, reducing localization accuracy. These challenges limit the reliability of FMCW-based defect localization methods.

Previous FMCW-based studies were carried out to validate cable diagnostics under isolated or idealized terminal conditions, leaving the effect of connected equipment unexamined.[14,15] In this study, we combine a distributed-parameter cable model with a high-frequency equivalent circuit of the terminal transformer and validate the combined model through live experiments on an energized 8.7/10 kV YJV cable [copper conductor cable with XLPE insulation and polyvinyl chloride (PVC) sheath], using noninvasive high-frequency current transformer (HFCT) and high-voltage coupling capacitor (HVCC) interfaces. By this method, we examined how terminal equipment perturbs defect-related and boundary-related reflections differently and found that defect reflections behave as independent local scattering centers, whereas terminal reflections are governed by transformer parasitics. This selective-sensitivity result provides a basis to separate genuine defect signals from equipment-induced artifacts and shows that FMCW sensing can be deployed directly on in-service cables without idealized terminal conditions. The results serve as a basis for deploying FMCW sensing technology in resilient power distribution networks.

2. Method

2.1 Circuit model of FMCW method

The defect localization model developed in this study treats the distribution cable as a distributed impedance sensor, enabling the continuous monitoring of insulation conditions through electromagnetic wave propagation. Localized insulation defects act as impedance discontinuities that perturb the characteristic impedance Z_0 in the model. The FMCW method detects perturbations by analyzing the phase shift and frequency difference between transmitted and reflected waves. In the model, signal propagation in a lossy coaxial medium is governed by the propagation constant γ, expressed as

$$\gamma = \sqrt{(R + j\omega L)(G + j\omega C)} = \alpha + j\beta \ , \tag{1}$$

where R, L, G, and C denote the per-unit-length resistance, inductance, conductance, and capacitance of the cable, α represents the attenuation constant and β is the phase constant associated with wave velocity. Here, $\omega = 2\pi f$ denotes the instantaneous angular frequency of the injected FMCW diagnostic signal, which varies continuously across the frequency sweep bandwidth B ($f_0 \leq f \leq f_0 + B$), distinguishing it from the fixed 50 Hz power-frequency operating voltage.(21) The real part α represents the attenuation constant and the imaginary part β represents the phase constant. When the sensing wave encounters a localized dielectric change, a reflection occurs. The reflection coefficient Γ at the defect site is defined as

$$\Gamma = \frac{Z_d - Z_0}{Z_d + Z_0} \ , \tag{2}$$

where Z_d is the local impedance at the defect and Z_0 is the characteristic impedance of the healthy cable segment. The FMCW method extracts defect information by processing the time-of-flight encoded in the reflected spectrum.

For defect detection, the sensing signal must be injected and extracted through coupling interfaces of HFCTs or capacitive couplers.(22) The transfer function of these interfaces, $H_{sensor}(\omega)$, introduces attenuation and phase distortion that must be incorporated into the model. The received signal $S_{rec}(t)$ is expressed as

$$S_{rec}(t) = H_{sensor}(\omega) \cdot \Gamma \cdot e^{-2\gamma l} \cdot S_{trans}(t) , \tag{3}$$

where l is the distance to the defect and $S_{trans}(t)$ is the transmitted FMCW chirp signal. This equation presents the combined effect of cable parameters, defect impedance, and sensor interface characteristics on diagnostic accuracy. A continuous, linearly frequency-modulated sinusoidal waveform is applied to probe the cable dielectric. The transmitted signal $S_{trans}(t)$ is defined as

$$S_{trans}(t) = A\cos\left(2\pi f_0 t + \pi K t^2\right) \quad \left(0 \leq t \leq T\right), \tag{4}$$

where A denotes the voltage amplitude, f_0 represents the initial sweep frequency, T is the sweep period, and $K = B / T$ represents the sweep rate for bandwidth B. The reflected signal $S_{rec}(t)$ incorporates propagation delay $\tau = 2l / v$ from impedance discontinuity at distance l, where v represents the wave velocity. An analog frequency mixer multiplies $S_{rec}(t)$ with the reference signal $S_{ref}(t)$.(23) Subsequent low-pass filtering extracts the low-frequency beat signal $S_{beat}(t)$.

$$S_{beat}(t) = \frac{1}{2} A_{rec} \cos\left(2\pi K \tau t + 2\pi f_0 \tau - \pi K \tau^2\right) \tag{5}$$

The beat frequency $f_b = K\tau = 2Kl / v$ correlates linearly with distance l. Executing a fast Fourier transform (FFT) on $S_{beat}(t)$ converts the time-domain beat signal into the beat spectrum.

2.2 Experiment

To validate the developed model, we constructed an experimental platform, and experiments were conducted under realistic operating conditions. An emulation platform was constructed to implement the FMCW principle (Fig. 1). Figure 1 shows how temporal delay is converted into a measurable frequency shift, serving as the sensing clock. The difference between the transmitted (blue) and reflected (red) signals is used to determine distance. The sensing principle relies on the linear frequency modulation of a continuous wave, where the time delay of the reflection from an insulation defect is mapped to a beat frequency (f_b), enabling the high-precision localization of the sensing target.

To obtain signals from an 8.7/10 kV YJV distribution cable, widely used in urban electrical grids for medium-voltage transmission and composed of copper conductor, XLPE insulation, and PVC sheath, specialized hardware sensors were integrated into the system. Figure 2 shows the cross-sectional structure of the tested cable segment, following IEC 60502-2 specifications.[24] From the conductor outward, the cable comprises a stranded copper core, an inner semi-conducting conductor screen, XLPE dielectric insulation, an outer semi-conducting insulation screen, a metallic copper tape screen, and an outer PVC protective sheath. High-frequency sensing waves propagate through the core conductor, with the XLPE dielectric acting as the distributed sensing medium.

The experimental platform integrated two complementary sensors for signal acquisition and injection. HFCT was clamped around the cable's ground lead, providing a noncontact sensing interface with a 100 kHz–50 MHz frequency response that covers the FMCW sweep bandwidth. The FMCW excitation signal was injected through HVCC, which acts as a high-pass filter to

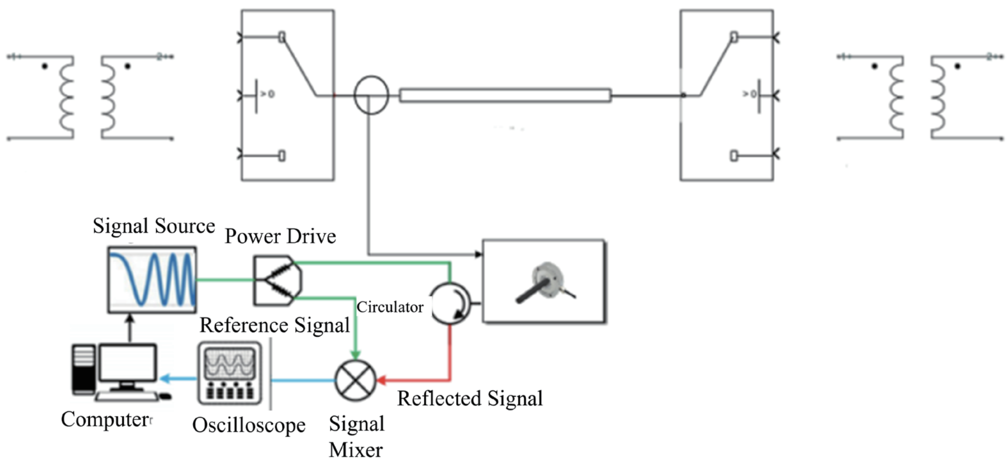

Fig. 1. (Color online) FMCW sensing principle showing the linear frequency modulation and the generation of the beat frequency (f_b) from the defect target.

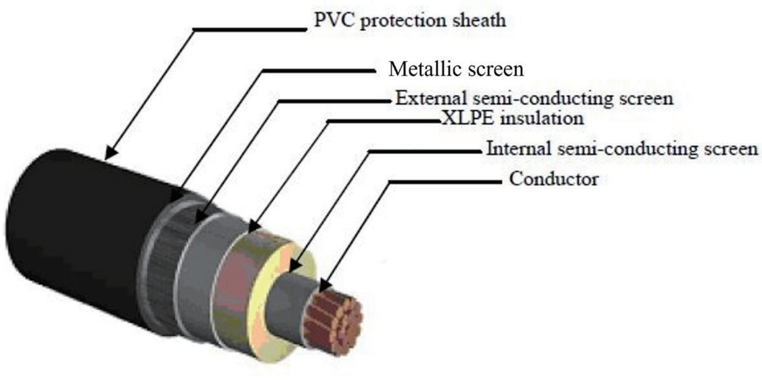

Fig. 2. (Color online) Cross-sectional structure and layer configuration of 8.7/10 kV YJV XLPE distribution cable.[25]

block the 50 Hz power component, transmitting high-frequency diagnostic signals.[26] The 96 m XLPE cable was used as a distributed sensing medium modeled by the equivalent circuit in Fig. 3.

Any change in cable condition manifests as an impedance variation. A localized insulation defect introduced 22 m from the cable head disturbs the characteristic impedance Z_0, generating reflection peaks for defect localization. The distributed impedance model represents the cable as a sequence of lumped elements per unit length: resistance R_0, inductance L_0, conductance G_0, and capacitance C_0. Within the defect region, these parameters change to R_1, L_1, G_1, and C_1. Boundary effects are modeled by ground conductance G_g, terminal capacitance C_t, and series inductance L_s, ensuring consistency with the simulation and accurate representation of insulation degradation. The high-frequency equivalent circuit of the transformer was constructed to define the complex impedance boundary encountered by the sensing wave (Fig. 4). It included ground capacitance C_g, inter-turn capacitance C_t, leakage inductance L_s, and high-frequency resistance R_s. These elements were used to determine the input impedance Z_{in} seen by the cable terminal.

Accurate defect localization requires impedance matching or compensation for mismatches introduced by Z_{in}. This transformer model evaluates how terminal equipment, acting as a complex sensing boundary, affects the signal-to-noise ratio and reflection characteristics at the sensing interface. The combined cable and transformer models ensure that the FMCW-based diagnostic system captures both distributed and boundary effects with high fidelity.

The artificial defect located 22 m from the cable head was evaluated under both circuit simulation and physical experimental conditions. In the experiment on the 96 m YJV cable, the defect was created by introducing a precise circumferential radial notch (1.5 mm width, 2.0 mm depth) into the outer semi-conducting layer and primary XLPE dielectric insulation. This simulated a localized mechanical defect commonly caused by physical impact or thermal expansion stress. In the equivalent circuit model, the defect was represented across a 0.1 m cable segment by reducing the per-unit-length capacitance ($C_{defect} = C_0 - \Delta C$) and increasing the conductance ($G_{defect} = G_0 + \Delta G$) to capture the localized dielectric permittivity drop and high-frequency dissipation at the crack boundary.[27] This localized impedance discontinuity, defined

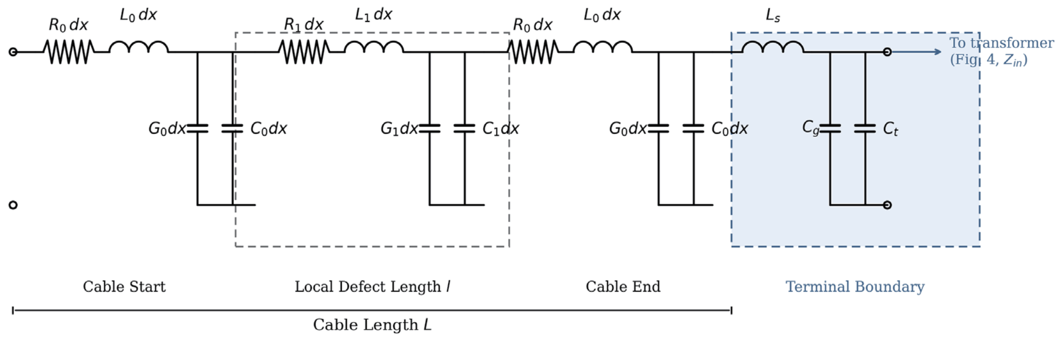

Fig. 3. (Color online) Distributed impedance model of XLPE cable, extended with the terminal boundary elements (C_g, C_t, and L_s) of connected transformer (drawn using AI).

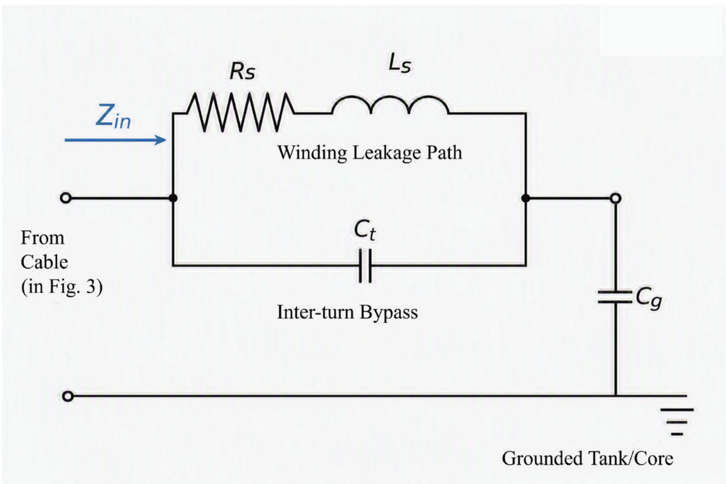

Fig. 4. (Color online) High-frequency equivalent transformer circuit (R_s, L_s, C_t, and C_g), defining input impedance Z_{in} to cable terminal (drawn using AI).

as Eq. (6), leads to the generation of the high-frequency diagnostic reflections required for FMCW localization.

$$\Delta Z = \sqrt{\frac{R + j\omega L}{G_{defect} + j\omega C_{defect}}} - Z_0 \tag{6}$$

Here, ΔZ denotes the localized impedance discontinuity (Ω) at the defect boundary, Z_0 is the nominal characteristic impedance (Ω) of the healthy cable segment, and R and L represent the per-unit-length series resistance (Ω/m) and inductance (H/m) of the conductor, respectively, G_{defect} and C_{defect} denote the modified per-unit-length conductance (S/m) and capacitance (F/m), respectively, across the damaged XLPE insulation segment, $\omega = 2\pi f$ is the instantaneous angular frequency (rad/s) of the swept FMCW signal, and j represents the imaginary unit.

The overall configuration and signal processing logic are shown in Fig. 5, which integrates equivalent circuit simulation, sensor data acquisition, and FMCW-based defect localization. The platform consists of a signal generation module (vector signal generator), a signal injection–extraction module (HVCC and HFCT), and a high-speed data acquisition unit. The generated FMCW chirp is divided by a power divider. One branch serves as the reference and the other is injected into the cable. A circulator ensures directional separation, protecting the sensing hardware from high-power reflections. The reflected signal, captured by the HFCT sensor, is mixed with the reference to produce an intermediate-frequency signal, which is digitized and processed by frequency-domain analysis to extract the defect location. To test robustness, two operating conditions were compared: one with the cable connected to a distribution transformer (complex boundary case) and one without (reference case). All parameters, including sweep bandwidth and power levels, were kept constant across multiple repetitions to quantify the model's immunity to terminal impedance variations.

Finally, to validate the FMCW diagnostic model empirically, experiments were conducted on the energized 96 m, 8.7/10 kV single-core YJV XLPE power cable testbed. The controlled mechanical notch introduced 22.0 m from the cable head confirmed that the FMCW method reliably detects localized insulation defects under live operating conditions.[28]

3. Results

3.1 Defect localization

The frequency-domain analysis further validates the sensing model under different boundary conditions. Figure 6 shows the FMCW defect localization spectra obtained from isolated and transformer-coupled configurations. Each configuration includes five repeated measurements, Transformer 1–5 and Normal Connection 1–5, performed under identical experimental

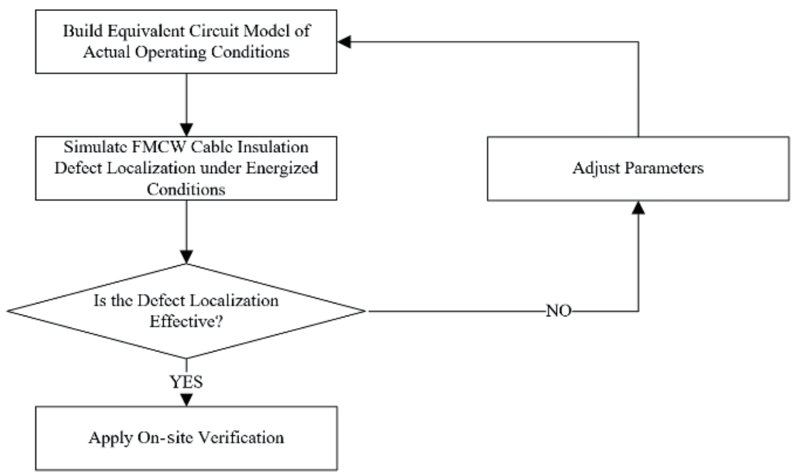

Fig. 5. (Color online) Sensing system logic, integrating circuit simulation, sensor data acquisition, and FMCW-based defect localization.

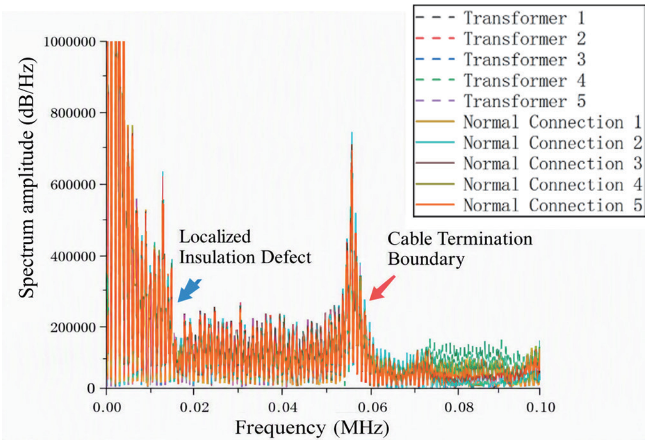

Fig. 6. (Color online) FMCW defect localization spectra obtained under isolated and transformer-coupled boundary conditions. Solid lines (Normal Connection 1–5) represent five repeated measurements of the isolated cable configuration, whereas dashed lines (Transformer 1–5) represent five repeated measurements with transformer coupling (left arrow: localized insulation defect at approximately 0.013 MHz, right arrow: cable termination boundary at approximately 0.056 MHz).

conditions to verify the repeatability and stability of the FMCW spectral response. The dashed lines represent transformer-coupled cases, whereas the solid lines represent isolated (normal connection) cases.

The callout arrows in Fig. 6 indicate two distinct reflection features. The first peak, marked by the left arrow at 0.013 MHz, corresponds to the localized insulation defect situated 22 m along the cable. The second major peak, marked by the right arrow at 0.056 MHz, corresponds to the total cable termination boundary. Under the isolated condition, the reflection peaks are sharp and well-defined, indicating minimal boundary interference and high sensitivity to impedance changes along the cable. When the transformer is connected, the spectra exhibit amplitude attenuation and slight peak shifts caused by the transformer's parasitic elements, particularly the ground capacitance C_g, inter-turn capacitance C_t, leakage inductance L_s, and high-frequency resistance R_s. These parameters collectively alter the input impedance Z_{in}, introducing signal damping and phase distortion that reduce localization precision.

Despite these effects, the FMCW method maintains identifiable reflection peaks corresponding to the defect position, confirming its robustness under realistic boundary conditions. The comparison highlights that transformer coupling primarily affects signal amplitude rather than fundamental localization frequency, demonstrating that impedance compensation or adaptive calibration can effectively restore diagnostic accuracy. This consistency between simulation and experiment supports the validity of the distributed impedance and transformer boundary models shown in Figs. 3 and 4, ensuring reliable defect detection across varying operational environments.

To extend this analysis beyond transformer coupling, the terminal boundary conditions were examined in open-circuit and short-circuit terminations, which are extreme configurations (Fig. 7). In the open-circuit termination, the termination caused a strong reflection peak at 0.056 MHz with minimal phase shift, whereas the localized defect at 0.013 MHz remains sharp and well-defined. In contrast, the short-circuit termination showed an inverted reflection at the same

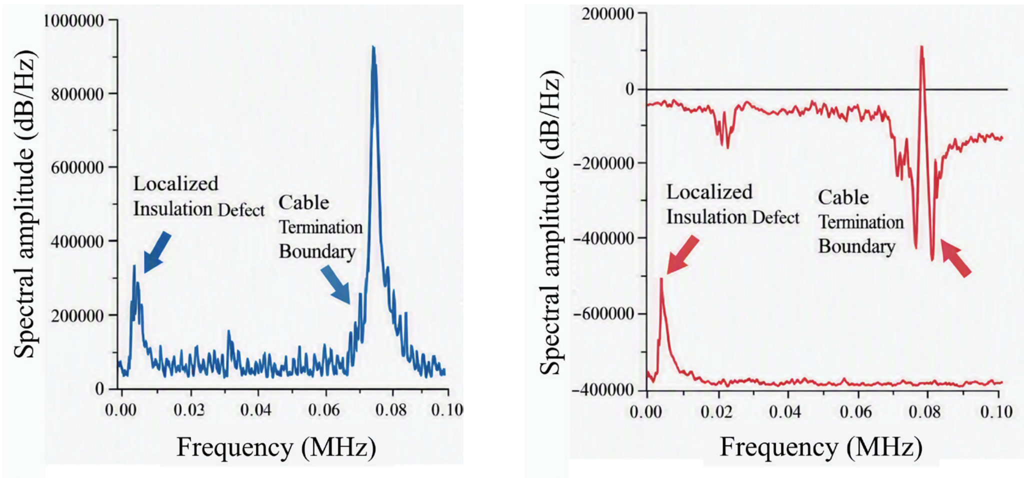

(a) (b)

Fig. 7. (Color online) FMCW defect localization spectra for (a) open-circuit and (b) short-circuit cable terminations.

frequency with reduced amplitude, resulting from impedance inversion at the boundary. These complementary spectra represent the two extreme termination conditions, confirming that the transformer-coupled response occurs between them (Fig. 6). Such a comparison result supports the impedance boundary model and shows that the FMCW method accurately distinguishes termination types, maintaining reliable defect localization performance under varying boundary configurations.

3.2 Robustness in defect localization

The relative percentage decrease was calculated using the standard peak extraction and spectral reduction methodology in FMCW reflectometry.[29]

$$\Delta A = \frac{A_{baseline} - A_{transformer}}{A_{baseline}} \times 100\% \tag{7}$$

Here, ΔA is the relative percentage decrease in reflection peak amplitude caused by transformer connection, $A_{baseline}$ is the peak spectral amplitude measured under normal connection conditions without connected terminal equipment, and $A_{transformer}$ is the peak spectral amplitude measured when the cable terminal is connected to the distribution transformer. For the localized defect peak at 0.013 MHz, curve fitting yielded the following results:

$$A_{baseline} = 609882.47\,\text{dB/Hz}\,, \tag{8}$$

$$A_{transformer} = 604785.75\,\text{dB/Hz}\,, \tag{9}$$

$$\Delta A_{defect} = \frac{609882.47 - 604785.75}{609882.47} \times 100\% = 0.836\% . \tag{10}$$

For the terminal reflection peak at 0.056 MHz, curve fitting yielded the following results:

$$A_{baseline} = 701506.41 \text{dB/Hz} , \tag{11}$$

$$A_{transformer} = 647010.71 \text{dB/Hz} , \tag{12}$$

$$\Delta A_{terminal} = \frac{701506.41 - 647010.71}{701506.41} \times 100\% = 7.768\% . \tag{13}$$

These values demonstrate that transformer parasitics attenuate global boundary reflections, leaving localized defect reflections largely intact. As a result, the FMCW method reliably detects insulation defects even when the cable is connected to complex equipment. This consistency between baseline and transformer-coupled conditions underscores the validity of the distributed impedance and transformer boundary models and supports the method's applicability in practical diagnostic environments. To calculate the raw spectrum beat frequencies (f_b) to defect locations (x), the FMCW range equation was used.(30,31)

$$x = \frac{v \cdot f_b \cdot T}{2B} \tag{14}$$

Here, v represents the propagation velocity in XLPE (1.72×10^8 m/s), B represents the FMCW sweep bandwidth (100 MHz), and T represents the sweep duration (1 ms). The extracted peak frequency at $f_b = 0.013$ MHz corresponds to the localized defect distance of approximately 22 m. The percentage reduction in reflection peak amplitude (ΔA) caused by transformer coupling is calculated using Eq. (7).

Table 1 shows the extracted peak beat frequencies, converted distance measurements, raw peak amplitudes, and calculated relative amplitude reductions across both defect and terminal boundaries. The measurements obtained from the physical cable test demonstrated excellent agreement with the equivalent circuit simulation results. Across thirty repeated experimental

Table 1
Comparison of defect localization of FMCW method in different connections.

Reflection feature	Localized defect peak	Terminal boundary peak
Peak beat frequency (f_b, MHz)	0.0130	0.0562
Calculated distance (m)	22.12	96.34
Actual distance (m)	22.00	96.00
Baseline amplitude (dB/Hz)	609882.47	701506.41
Transformer amplitude (dB/Hz)	604785.75	647010.71
Amplitude decrease (ΔA) (%)	0.836	7.768

trials, the FMCW system consistently located the 2.0 mm deep physical notch at a measured distance of 22.18 m (standard deviation = 0.11 m), corresponding to a relative error of 0.82%. This indicates that the practical implementation of FMCW defect localization poses no operational difficulties and effectively detects subtle insulation cuts even under energized transformer-coupled conditions.

In addition to accurate distance estimation, the transformer connection produced a 7.77% reduction in the amplitude of the terminal reflection peak at 0.056 MHz, reflecting a significant modification of boundary impedance due to parasitic elements, as shown in Table 1. This reduction arises from partial energy absorption and impedance mismatch introduced by the transformer's high-frequency equivalent network. By contrast, the defect-related reflection peak at 0.013 MHz exhibited only a 0.836% decrease, confirming that defect-induced reflections are governed primarily by local impedance discontinuities along the cable and are only weakly affected by terminal boundary conditions. These results ensure reliable detection across varying operational environments, whereas transformer parasitics attenuate global boundary reflections, and localized defect reflections remain robust.

3.3 Defect reflection

The defect-induced peaks are shown in Fig. 8. The figure also shows the effect of transformer integration on distinct reflection components. The amplitude and characteristic frequency of the defect peak remain nearly unchanged under the two operating conditions, confirming the high robustness of the sensing mechanism against terminal impedance variation. This stability is critical for sensor applications, as early-stage insulation defects typically generate weak reflection signatures that are easily obscured. The developed FMCW sensing platform consistently resolves these peaks and ensures reliable target detection in complex, energized environments.

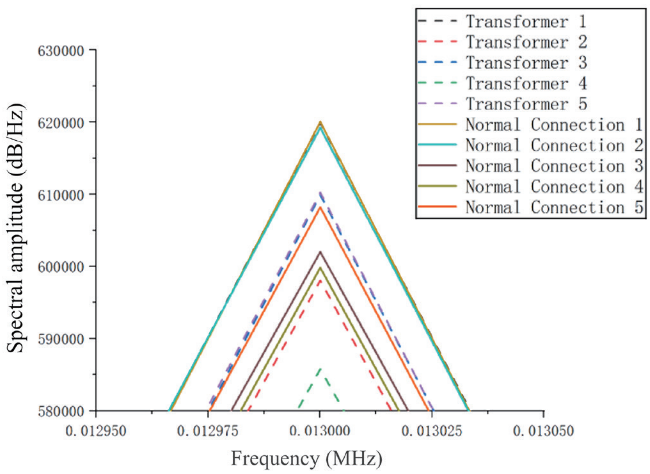

Fig. 8. (Color online) Defect-induced frequency peaks demonstrating high selectivity and stability against terminal impedance variations.

In contrast, the terminal reflection peaks show a significant amplitude reduction when the transformer is connected (Fig. 9). The sensitivity of boundary reflections to terminal impedance characteristics underscores the necessity of modeling connected equipment within the sensing framework. For practical sensor deployment, these results show that boundary reflections must be characterized to maintain the integrity of the global diagnostic profile and avoid the underestimation of defect severity.

3.4 Trend analysis

The fitted curves for defect peaks show minimal variation across operating conditions, confirming the stability of the FMCW method (Figs. 10 and 11). This independence ensures that the sensing mechanism remains reliable for defect localization regardless of the terminal equipment used. By contrast, the fitted curves for terminal peaks show significant downward trends when the transformer is connected, confirming the strong effect of boundary impedance on termination reflections. For sensor applications, the FMCW-based systems must incorporate transformer-equivalent models to correctly interpret termination signals. Without such modeling, boundary reflections may mask or distort defect-related information.

The experimental results demonstrate that the FMCW method enables robust defect localization under energized conditions, with defect reflections largely unaffected by transformer coupling. This robustness proves the cable-as-sensor concept, showing that localized impedance discontinuities can be reliably detected even in complex network environments. At the same time, the sensitivity of terminal reflections to transformer parasitics underscores the necessity of integrating sensor interface modeling and transformer-equivalent circuits into FMCW diagnostic schemes. FMCW signals consistently show defect peaks, ensuring the reliable identification of early-stage insulation degradation, whereas terminal reflections are strongly affected by connected equipment, requiring careful modeling and interpretation for accurate field

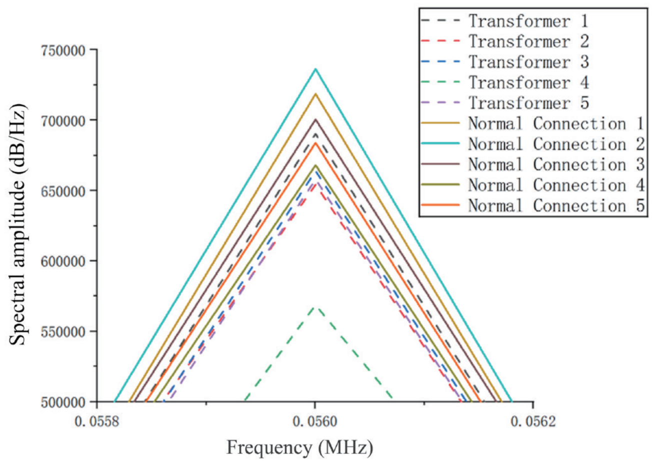

Fig. 9. (Color online) Termination reflection peaks showing sensitivity of sensing interface to global system boundary changes.

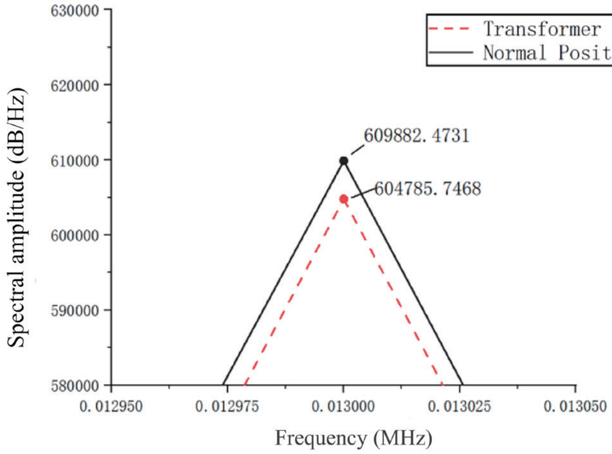

Fig. 10. (Color online) Curve fitting of defect localization peaks showing consistency of distributed sensing target across varying network topologies.

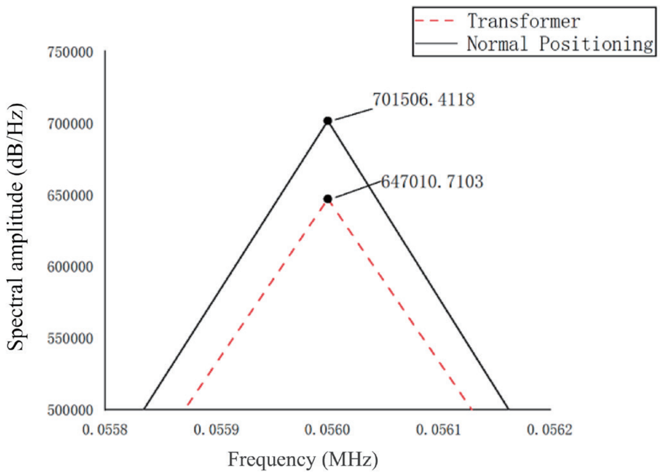

Fig. 11. (Color online) Curve fitting of termination peaks showing attenuation trend caused by complex impedance of sensing boundary.

deployment. Therefore, the experimental results validate the feasibility of FMCW-based cable diagnostics and provide a reference for sensor design and application in real-world distribution networks.

3.5 Statistical variability and accuracy

To evaluate measurement repeatability and quantify localization uncertainty, 30 independent test trials were conducted on isolated baseline and energized transformer-coupled operating states.[32] The sample mean ($\bar{x}$), standard deviation (σ), and two-sided 95% confidence interval (CI) were computed as follows.

$$95\%\ CI = \overline{x} \pm t_{0.025,N-1} \cdot \left(\frac{\sigma}{\sqrt{N}}\right) \tag{15}$$

Here, $t_{0.025,29}$ = 2.045 represents the critical value from Student's *t*-distribution. Table 2 shows the statistics of 30 trial runs for the true defect distance of 22.0 m. The standard deviation remained within ≤ 0.11 m, and the upper bound of the 95% *CI* yields a maximum relative error below 1.0%. Such a narrow confidence interval indicates high system stability and proves that terminal impedance disturbances do not induce significant statistical variance in FMCW defect localization.

An advantage of the developed FMCW method over BIS is its ultralow computational complexity and real-time execution capability.[33] BIS requires discrete point-by-point frequency steps and iterative optimization routines, whereas FMCW processing relies primarily on a single-pass 1D FFT. Table 3 shows the breakdown of execution latency measured on a standard digital processing platform (ARM Cortex-M7 microcontroller/dual-core host digital signal processor operating at 480 MHz). The total end-to-end elapsed time from initial signal injection to the final defect distance calculation is 14.78 ms, enabling online real-time monitoring update rates exceeding 65 Hz. This rapid response time confirms the suitability of the developed system for continuous, automated online fault diagnostics in live distribution networks.

4. Discussion

The results of this study show the robustness of the FMCW method in distinguishing the reflection behaviors of insulation defects and cable terminations under varying boundary conditions. In the experiment, defect-induced reflection peaks remained stable in both amplitude and spectral position when the cable termination was connected to a transformer, whereas terminal reflection peaks exhibited pronounced attenuation. This difference arises from the

Table 2
Statistical analysis of defect localization accuracy of 30 test trials.

Operating condition	Actual location (m)	Mean measured location (m)	Standard deviation (m)	95% *CI* (m)	Mean absolute error (m)	Mean relative error (%)
Baseline	22.00	22.12	0.08	[22.09, 22.15]	0.12	0.55
Transformer	22.00	22.18	0.11	[22.14, 22.22]	0.18	0.82

Table 3
End-to-end processing latency breakdown for FMCW defect distance estimation.

Processing stage	Operation	Execution time (ms)
1. Data acquisition	Single FMCW chirp sweep duration	1.00
2. Buffer transfer	DMA transfer of 10,000 sampling points	1.20
3. Spectral analysis	Hanning windowing 216-point FFT	10.40
4. Peak detection	Thresholding and parabolic peak interpolation	2.10
5. Distance mapping	Evaluation range	0.08
Total elapsed latency	End-to-end real-time execution time	14.78

physical nature of the impedance discontinuities responsible for these reflections. Insulation defects introduce localized variations in distributed electrical parameters such as capacitance and conductance, which act as independent scattering centers for FMCW signals. Consequently, defect reflections are governed by local impedance contrast and are only weakly affected by terminal boundary conditions. In contrast, terminal reflections depend directly on the equivalent impedance presented at the cable end, which is strongly modified by transformer parasitics, leading to partial energy absorption and impedance matching effects.

This distinction highlights a key advantage of FMCW-based sensing compared with conventional reflectometry methods. TDR is highly sensitive to termination conditions, with boundary impedance changes often causing severe waveform distortion and localization errors. Similarly, BIS suffers from spectral distortion owing to terminal impedance variation, complicating defect interpretation. In FMCW-based localization, propagation delay information is mapped into the frequency domain, enabling partial decoupling between localization accuracy and amplitude variation. As a result, defect localization remains stable even when boundary conditions change, as confirmed by the robustness observed in this study.

The results of this study support the cable-as-sensor concept, where localized impedance discontinuities become natural sensing targets. The robustness of defect reflections ensures that early-stage insulation degradation can be reliably detected even in complex, energized environments. This capability is particularly important for smart grid applications, where online monitoring must be performed without interrupting power supply or modifying network topology. At the same time, boundary reflections remain sensitive to the connected equipment, underscoring the necessity of incorporating transformer-equivalent models and coupling sensor interfaces into the FMCW method to maintain the integrity of the global sensing profile.

For field deployment, this robustness simplifies sensor installation and reduces operational costs, enabling standardized diagnostic workflows that are independent of specific network configurations. Nevertheless, limitations must be acknowledged: the present experiments and simulations were conducted on a single 8.7/10 kV YJV XLPE cable with one transformer termination. Real-world distribution networks often involve multiple devices, tee-branches, and varying dielectric aging profiles, making the precise modeling of parasitic parameters (R_s, L_s, C_t, and C_g) challenging. Future research should therefore focus on high-frequency parameter identification for diverse grid assets and multi-branch echo separation algorithms to extend FMCW diagnostic generalizability across complex, multi-terminal networks.[34] To achieve grid integration, the following standardized transformer-equivalent modeling framework is required.[35]

- Standardized high-frequency asset parameterization: Substation transformers can be precharacterized into model classes on the basis of voltage rating and winding topology, with scattering parameters measured to define equivalent parasitic elements.
- Adaptive terminal calibration: FMCW diagnostic software can track terminal echo attenuation as an online calibration metric, dynamically updating termination impedance parameters without taking transformers offline.

- Automated spectral decoupling: By integrating standardized model libraries into diagnostic hardware, the real-time subtraction of complex terminal reflections can be performed, enabling the operator-independent identification of localized defect peaks.

Finally, environmental and structural factors such as thermal variations, dielectric aging, and multi-device connections introduce additional complexity.(36) Adaptive signal processing and AI-driven spectral analysis frameworks, such as dynamic dispersion compensation, temperature-calibrated velocity tracking, and machine learning models (convolutional neural networks combined with long short-term memory networks), can be employed to distinguish defect reflections from multi-terminal echoes and background noise. These adaptive models enable robust defect localization and low false-positive rates in heterogeneous field environments.

5. Conclusion

An FMCW-based defect detection and localization method was developed and validated for partial insulation defects in power distribution cables. The diagnostic method integrates high-frequency signal injection, propagation analysis, echo extraction, and matched-filter-based delay estimation. Energized experiments on 96 m YJV XLPE cables confirmed that the system consistently located a 2.0 mm deep notch at 22.18 m with a standard deviation of 0.11 m, showing a relative error of 0.82% across 30 trials. The test results showed that transformer connection attenuates terminal reflections significantly (7.768% amplitude reduction at 0.056 MHz), whereas defect-induced peaks remain nearly unchanged (0.836% reduction at 0.013 MHz), demonstrating selective sensitivity between global and local reflections. Localization error remained within 5% under both isolated and transformer-coupled conditions, confirming strong robustness under practical equipment-connection scenarios.

The results validate the cable-as-sensor concept, showing that localized defect reflections are decoupled from terminal impedance variations. The demonstrated robustness enables reliable online monitoring in energized networks, reducing operational costs and supporting scalable deployment in smart grids. It is necessary to extend this method to multi-equipment coupling scenarios, adaptive spectral-separation techniques, and AI-driven signal processing to enhance defect severity assessment and generalize FMCW diagnostics across complex distribution topologies.

References

1 X. J. Rao, Z. L. Xu, Y. Q. Ding, X. Y. Hu, and K. Zhou: Trans. China Electrotech. Soc. **40** (2025) 1628. https://doi.org/10.19595/j.cnki.1000-6753.tces.240274

2 Y. Hao, P. Zhao, B. Hui, Y. Cheng, W. Zhu, M. Fu, and X. Li: High Volt. **8** (2023) 967. https://doi.org/10.1049/hve2.12320

3 B. Shan, C. Du, J. Cheng, W. Wang, and C. Li: Polymers **14** (2022) 5478. https://doi.org/10.3390/polym14245478

4 J. Yang, R. Li, L. Hu, and W. Wang : Polymers **16** (2024) 1600. https://doi.org/10.3390/polym16111600

5 Y. Li, R. Zhao, Y. Liu, H. Li, Q. Yue, and H. Chen: Autom. Constr. **183** (2026) 1406784. https://doi.org/10.1016/j.autcon.2026.106784

6 B. Wang, S. Li, J. Peng, J. Deng, X. Zhao, and H. Sun: IEEE Trans. Instrum. Meas. **74** (2025) 1. https://doi.org/10.1109/TIM.2025.3579848

7 D. Zhang, H. Lu, R. Han, J. Sheng, Z. Wang, and C. Xu: Sens. Mater. **38** (2026) 2217.

8 Y. La, L. B. Tian, J. H. Ye, and J. L. Wang: Adv. Mater. Res. **490** (2012) 3449. https://doi.org/10.4028/www.scientific.net/amr.490-495.3449
9 G. Cerri, R. De Leo, L. Della Nebbia, S. Pennesi, V. Mariani Primiani, and P. Russo : IEE Proc. - Sci. Meas. Technol. **152** (2005) 217. https://doi.org/10.1049/ip-smt:20045035
10 N. Hirai, T. Yamada, and Y. Ohki: Proc. IEEE Int. Conf. Condition Monitoring and Diagnosis (IEEE, 2012) 229. https://doi.org/10.1109/CMD.2012.6416417
11 B. Shan, S. Li, L. Yu, W. Wang, C. Li, and X. Meng: IEEE Access **9** (2021) 154755. https://ieeexplore.ieee.org/stamp/stamp.jsp?arnumber=9551967
12 P. F. Fantoni: Proc. 9th Int. Conf. Insulated Power Cables (JICABLE, 2015) 1. https://www.jicable.org/TOUT_JICABLE_FIRST_PAGE/2015/2015-C5-4_page1.pdf.
13 T. Yamada, N. Hirai, and Y. Ohki: Proc. 2012 IEEE Int. Conf. Condition Monitoring and Diagnosis (IEEE, 2012) 677. https://doi.org/10.1109/CMD.2012.6416236
14 D. Zhang, X. Liang, Z. wang, D. Dong, Z, Wang, and J. Yang: Proc. 2025 Int. Conf. Artificial Intelligence, Electrical and Electronic Engineering (AI3E, 2025) 176. https://doi.ieeecomputersociety.org/10.1109/AI3E69313.2025.00042
15 B. Wang, S. Li, J. Peng, J. Deng, X. Zhao, and H. Sun: IEEE. Trans. Instrum. Meas. **74** (2025) 11. https://doi.org/10.1109/TIM.2025.3579848
16 G. Frusque, D. Mitchell, J. Blanche, D. Flynn, and O. Fink: Mech. Syst. Signal Process. **208** (2024) 111022. https://doi.org/10.1016/j.ymssp.2023.111022
17 K. Jiang, K. Zhou, X. Ren, and Y. Xu: Energies **18** (2025) 2428. https://doi.org/10.3390/en18102428
18 Z. Cheng, H. Mu, X. Zou, C. Song, R. Wang, and K. Fan: IEEE Trans. Dielectr. Electr. Insul. **33** (2025) 1. https://doi.org/10.1109/TDEI.2025.3625111
19 S. Li, B. Wang, J. Peng, Z. Jiang, J. Deng, X. Zhao, and H. Sun: Electr. Power, Syst. Res. **252** (2026) 112374. https://doi.org/10.1016/j.epsr.2025.112374
20 R. Li, K. Zhou, H. Wan, and X. Rao: Trans. China Electrotech. Soc. **36** (2021) 1743. https://dgjsxb.ces-transaction.com/EN/10.19595/j.cnki.1000-6753.tces.200144
21 T. B. Arabi and T. K. Sarkar: Proc. 31st ARFTG Conf. Digest (IEEE, 1988) 45. https://doi.org/10.1109/ARFTG.1988.323901
22 X. Zou, H. Mu, L. Qu, H. Zhang, C. Xie, and G. Zhang: Energy Rep. **8** (2022) 1474. https://doi.org/10.1016/j.egyr.2022.02.202
23 J. Lee and T. H. Yoon: AIP Adv. **2** (2012) 022170. https://doi.org/10.1063/1.4733344
24 International Electrotechnical Commission: https://www.iecee.org/certification/iec-standards/iec-60502-22014 (accessed July 2026).
25 EM Works: https://www.emworks.com/application/how-does-thermal-behavior-affect-xlpe-cable-performance (accessed July 2026).
26 L. Della Giovanna, F. Guastavino, and E. Torello: Metrology **6** (2026) 24. https://doi.org/10.3390/metrology6020024
27 H.-S. Kim, J. Jung, and B.-W. Lee: Energies **17** (2024) 2024. https://doi.org/10.3390/en17092024
28 Y. Xu, S. Zhang, and Y. Wu: Energies **19** (2026) 2092. https://doi.org/10.3390/en19092092.
29 X. Wang, Z. Wang, J. P. Vreuls, and B. Zhang: IEEE Trans. Consum. Electron. **71** (2025) 6880. https://doi.org/10.1109/TCE.2024.3442817
30 D. Zhang, X. Liang, Z. Wang, D. Dong, Z. Wang, and J. Yang: Proc. 2025 Int. Conf. Artificial Intelligence, Electrical and Electronic Engineering (AI3E) (IEEE, 2025) 176. https://doi.org/10.1109/AI3E69313.2025.00042
31 W. Zhu, B. Hui, J. Li, T. Han, L. Zhao, and S. Hou: Energies **18** (2025) 5346. https://doi.org/10.3390/en18205346.
32 E. R. Cohen: Meas. Sci. Technol. **9** (1998) 022. https://doi.org/10.1088/0957-0233/9/6/022
33 J. A. Park and S. C. Song: J. Korean Inst. Electromagn. Eng. Sci. **30** (2019) 88. https://doi.org/10.5515/KJKIEES.2019.30.1.88
34 W. Ben Hassen, M. Slimani, and F. Auzanneau: Meas. Sensors **43** (2026) 101981. https://doi.org/10.1016/j.measen.2025.101981.
35 S. Kingston, E. Benoit, A. S. Edun, F. Elyasichamazkoti, D. E. Sweeney, J. B. Harley, P. K. Kuhn, and C. M. Furse: Sensors **21** (2021) 5268. https://doi.org/10.3390/s21165268
36 L.-Q. Qu, H.-B. Mu, X.-Y. Zou, R.-J. Wang, X.-F. Zhao, and L. Pu: Energy Rep. **9** (2023) 904. https://doi.org/10.1016/j.egyr.2023.05.021